

## Research Article

# Investigation on Surface Wave Characteristic of Water Jet

**He Jie, Wang Jingjing , Liu Xiumei , Li Beibei , Li Wei , Gu Ming ,  
Xie Yongwei , Cai Zonghang , and Ma Jichao **

*School of Mechatronic Engineering, China University of Mining and Technology, Xuzhou 221116, China*

Correspondence should be addressed to Liu Xiumei; liuxiumei\_lxm@126.com

Received 9 December 2018; Revised 4 March 2019; Accepted 24 March 2019; Published 10 April 2019

Academic Editor: Mostafa S. Shadloo

Copyright © 2019 He Jie et al. This is an open access article distributed under the Creative Commons Attribution License, which permits unrestricted use, distribution, and reproduction in any medium, provided the original work is properly cited.

Water jet surface stability is important to enhance fighting efficiency of fire water monitor. In this paper, a visualization experimental method is designed to capture the surface waves of water jet out from fire water monitor, and the wavelength and the amplitudes are captured and measured from the obtained water jet images. The Sobel horizontal gradient direction template and Burg method are selected to obtain wavelength characteristic of water jet. Based on surface morphology, the relationship between wave characteristic of water jet and Weber number is also discussed. The structure of the surface wave changes from cosmic turbulence to stochastic small-scale waves with increasing Weber number and becomes fully chaotic finally. The average wavelength of water jet out from fire water monitor decreases with increasing Weber number. The growth rate in the presence of wavelength with the lower  $We_g$  is less than that of the higher  $We_g$ . Furthermore, the amplitudes of the water jet increase continuously with increasing flow distance and  $We_g$ . In other words, the larger the Weber number is, the faster the velocity of surface waves on water jet is. The main objective of the present work is to give the basis for better understanding the microstructure of water jet, which in turn improves the performance of fire water monitor.

## 1. Introduction

The water jet out from fire water monitor is commonly used to firefighting, cooling, heat insulation, and smoke exhaust in our life, and it has the advantage of less water consumption, being clean, and eliminating dust. When the water is ejected from the fire water monitor, the jet water column is in direct contact with the air and the jet surface fluctuates. When the fluctuation develops to a certain extent, droplets fall off the surface of the water column and water mist will be formed [1, 2]. The size, distribution, and velocity of water mist are often emphasized in the design of fire water monitor. The microstructure of the water jet is the key to the development of water mist, which directly affects the performance of fire water monitor. The wave characteristics of water jet remain a challenging topic.

Many scholars have carried out extensive research on water jet out from fire water monitor, but the related mechanism has not been well clarified so far. Numerically, Miyashita et al. [3] depicted the water discharge trajectory of a large-capacity monitor by a 3D simulation model based on the moving particle semi-implicit method, and they confirmed

that the detailed characteristics of the flying behavior and water discharge trajectory depend on the discharge flow and/or pressure. Hu et al. [4, 5] obtained the parameters on the optimal structure of fire water monitor based on the internal flow field of fire water monitor. Guha et al. [6, 7] and Zhang et al. [8, 9] studied the motion characteristics of high-pressure water jet in the air based on the multiphase flow model. Shinjo and Umemura [10, 11], as well as Fuster et al. [12], investigated the evolution of surface waves based on the large eddy simulation method, and the ligaments and droplets on the turbulent water jet surfaces have also been obtained. Although the numerical simulation method can well predict the motion characteristics of the water jet, wave characteristics of water jet could not be discussed in their works. An experimental method has also been carried out in the field of jet structure extraction [13, 14] and trajectory recognition [15]. For example, Mayer et al. [16], Ma et al. [17], and Ng et al. [18] studied the surface structure of a water jet by a high-speed camera. Portillo et al. [19] and Gong et al. [20, 21] measure the wavelength from the obtained jet images using the spectral method. Most of them only focus on long range, large flux, and the efficiency of fire water monitor;

characteristics of stability surface waves were not presented in their work.

Image processing is one of the most fundamental issues in analyzing the behaviors of water jet. Images obtained are often distorted during its acquisition, processing, compression, transmission, and reproduction. These distortions decrease the performance of visual and computerized analysis. It is clear that image signal extraction combined with power spectral method is an effective method for analysis after image denoising. The common power spectral methods are divided into two categories: the conventional power spectral method and the modern power spectral method. Welch method [22] is one of the conventional power spectral methods. A relevant water jet image processing method based on Welch method has been solely carried out by Portillo et al. [19] and Gong et al. [20, 23]. The computational formula of the Welch method is expressed as

$$\bar{P}(\omega) = \frac{1}{MUL} \sum_{i=1}^L \left| \sum_{n=0}^{M-1} x_{N'}^i(n) d(n) e^{-j\omega n} \right|^2 \quad (1)$$

where  $N$  is the number of data in random sequence,  $L$  is the number of the segments,  $M$  is the number of data in each segment,  $x(n)$  represents arbitrary data sets, and  $d(n)$  is the window function.  $U = (1/M) \sum_{n=0}^{M-1} d^2(n)$  is a normalizing factor used to achieve an asymptotic and unbiased estimation, and  $\omega$  is the circular frequency.  $\sum_{n=0}^{M-1} x_{N'}^i(n) d(n) e^{-j\omega n}$  is the Fourier transform of random sequence of segment  $i$ ,  $1 \leq i \leq L$ .

Instead of the Welch method, the Burg method is one of the modern power spectral methods. The Burg method is also used to measure surface waves of high-speed liquid jets [21], which is expressed as

$$P_x(e^{j\omega}) = \frac{\sigma^2}{\left| 1 + \sum_{k=1}^P a_k e^{-j\omega k} \right|^2} \quad (2)$$

where  $P$  is the degree of model,  $k = 1, 2, \dots, p$ , the reference value of  $P$  is  $N/3 < P < N/2$ , and  $N$  is the length of the sample.  $\sigma^2$  is the variance of white noise, and  $a_k$  is the coefficient.  $e^{-j\omega k} = \cos(\omega n) - j \sin(\omega n)$  is the complex sinusoidal, and  $\omega$  is circular frequency.

According to the principle of the Welch method, the result of the Welch method depends on the selection of window function. The most used window function is Blackman window, which has less sideband leakage but wider main lobe, and it indicates that the resolution of Blackman window is not sufficient [21]. However, the Burg method does not require window function. The Burg method uses data other than the known finite-length autocorrelation sequence according to the principle of maximum entropy. It uses the prediction extrapolation method instead of zero processing, and the resolution will be improved. And the Burg method is an adaptive spectral method, which does not depend on window function. The accuracy of the wavelength calculated by the Burg method has been verified in the literature [21]. With respect to the principle discussed here, the Burg method is better than the Welch method in our paper.

In this paper, a visualization experimental method is designed to capture the surface waves of water jet out from fire water monitor. The important parameters of the visualization experimental method are discussed. The Sobel horizontal gradient direction template is used to enhance the vertical boundary of the image, the Burg method was selected to measure the wavelength from the obtained image signals, and the evolution of water jet in the flow in both time and space is obtained. Furthermore, the relationship among the water jet wavelength, the amplitude, and Weber number is investigated based on quantitative information extracted from jet images.

## 2. Experimental Methods

Our experimental system is divided into two parts. The first part is the water jet system including water tank, centrifugal pump, pressure transmitter, flow transmitter, fire water monitor, and various control valves. The second part is the image acquisition system including high-speed camera, computer, light, and related processing software.

Figure 1(a) shows the physical diagram of the water jet system. The water jet system of the fire water monitor is powered by a centrifugal pump, which draws the water from the water tank into the pipelines. Water is ejected into the air through the fire water monitor and a water column will be formed. The frequency of the centrifugal pump is controlled by the frequency converter, and then the pressure and flow of the water jet will be changed. The diameter of pipelines, components, and flanges between the centrifugal pump and the fire water monitor in this water jet system is 80 mm.

Figure 1(b) shows the image acquisition system near the nozzle. Jet images are captured by a high-speed camera (the Phantom VEO-710L) with a 100mm F2.8 macro lens. This high-speed camera has a maximum frame rate of 68,000 fps and the camera's maximum global image size is 1280×800 pixels. The illumination is provided by an optical-fiber source (LA-100USW). The high-speed camera and the optical-fiber source are mounted at both sides of the nozzle, whose axis stands in the same horizontal plane. To avoid dynamic ambiguity, the highest frame rate and exposure time of the high-speed camera used in our experiment are 7500 fps and 1μs, respectively. The size of the global images obtained is 1280×800 pixels. The experimental resolution was 20 μm/pixel. The jet images are collected when the water jet is stable.

Figure 2 shows the structure of the fire water monitor used in our experiment. The nozzle is mounted on the monitor body through a threaded interface. The diameter of the inlet  $D$  is 64 mm, the diameter of the outlet  $d$  is 34 mm, and the length of the rectifier  $l$  is 34 mm. The contraction angle  $\theta$  is 5°. The spray angle of the fire water monitor in this experiment is set to 0°, that is, horizontal spray. The combined nozzle of the contraction section and the rectifier section can stabilize the flow and reduce the energy loss.

The water jet velocity at the outlet of the nozzle could be calculated by

$$U = \frac{Q}{A} \quad (3)$$

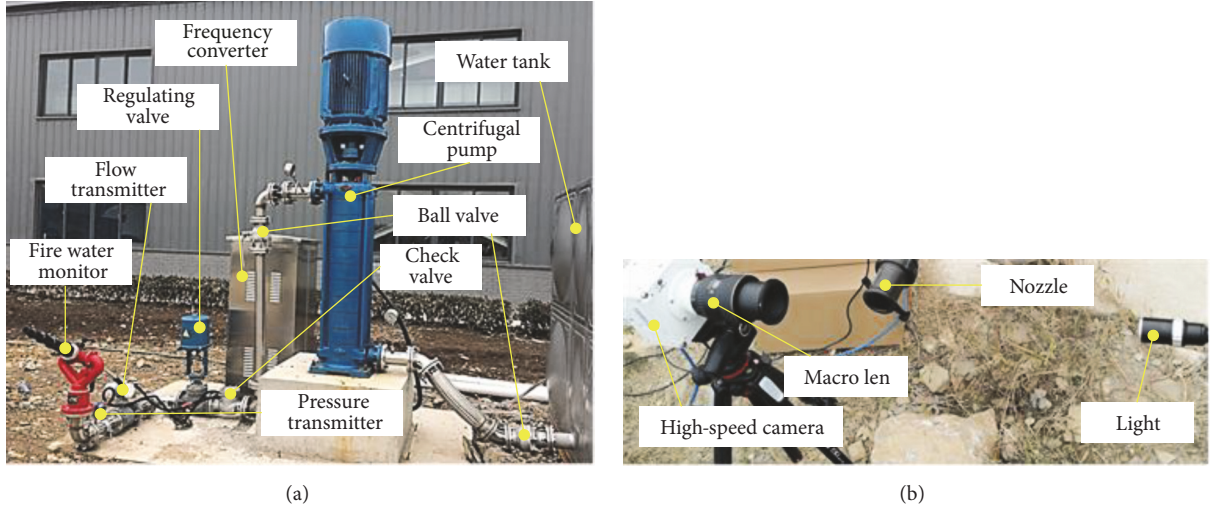


FIGURE 1: Experimental setup. (a) Physical diagram of the water jet system. (b) The image acquisition system near the nozzle.

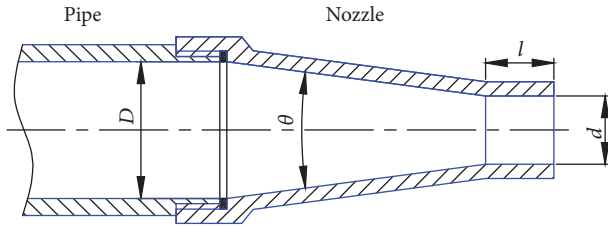


FIGURE 2: Schematics of the fire water monitor.

where  $Q$  is the flux recorded by the flow transmitter, and  $A$  is area of the outlet cross-section, defined as

$$A = \pi \left( \frac{d}{2} \right)^2. \quad (4)$$

The Weber number based on air density is calculated by

$$We_g = \frac{\rho_g U^2 d}{\sigma} \quad (5)$$

where  $\rho_g$  is the density of air, and  $\sigma$  is the surface tension of water.

Our experiment was conducted at room temperature. The flow conditions and the values of related parameters in our experiment are presented in Table 1.

### 3. Results

Microscopic structure of water jet out from fire water monitor is shown in Figure 3. It shows that continuous water jet is ejected from a round nozzle, and the water jet diverges significantly from the cylinder type on the axial direction later. There is surficial disturbance at the interface between water and air, and the amplitude of the disturbance increases in the downstream which could be seen from the contour of

TABLE 1: Parameters of fire water monitor in our experiment.

Parameter	Symbol	Value
Nozzle diameter	$d$	34 mm
Temperature	$T$	293 K
Liquid density	$\rho_L$	998 kg/m <sup>3</sup>
Air density	$\rho_g$	1.21 kg/m <sup>3</sup>
Jet velocity	$U$	3.41-17.58 m/s
surface tension	$\sigma$	0.07275 N/m
Weber number	$We_g$	6.99-139.55

the water jet in Figure 3(b). At the initial stage of jet injection, the shear stress at the boundary layer between water and air is very small, so there is almost no deformation of water jet surface near the nozzle exit. Then, surface velocity of the water jet increases, the shear at the water/air boundary layer is higher in magnitude [24], and the vortices will appear in the boundary layer induced by the Kelvin-Helmholtz instability. The low pressure produced by the vortices can lift the water/air boundary layer. When the lifting force is large enough to overcome the surface tension at the water/air boundary layer, the surface of the water jet begins to lose stability and produce weak protuberance and depression. Meanwhile, the K-H surface wave would be found on the water jet.

According to the anatomy of these high speed water jets in air, the water jet out from fire water monitor can theoretically be divided into three distinct regions, namely, the potential core region, the main region, and the diffused droplet region [1]. As potential core region is close to the nozzle exit, which is important to the stability and the efficiency of firefighting waters, we focus on surface wave of water jet in this potential core region. Figure 3(c) shows the enlarger area marked by the yellow line obtained in our experiments. After the water jet leaves the nozzle, the mass and momentum exchange

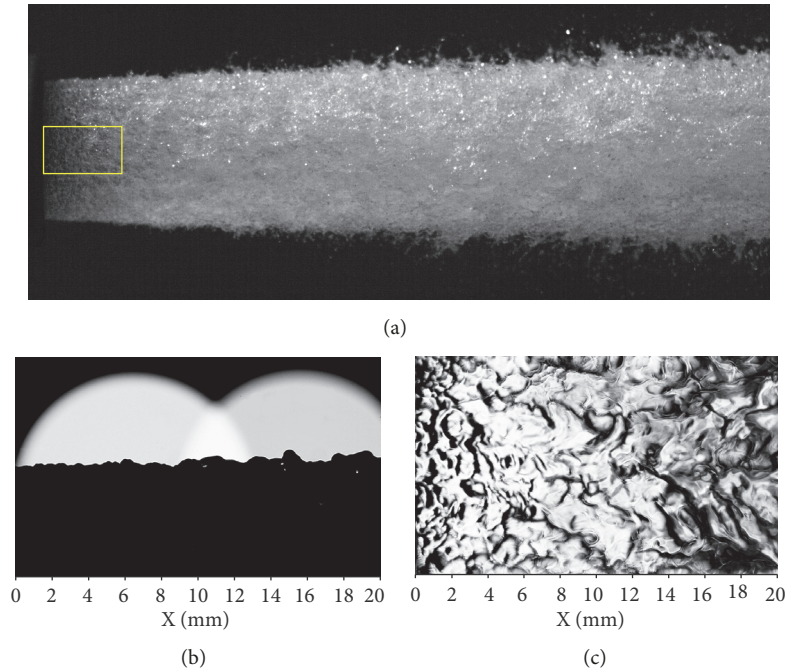


FIGURE 3: (a) Microscopic structures of water jet out from fire water monitor. (b) The contour of the water jet in the upper part. (c) Surface wave of enlarger area marked by the yellow line (the resolution is  $20 \mu\text{m}/\text{pixel}$ ).

will induce a great velocity difference at the boundary layer between water and air, and the K-H surface waves are clear enough later. Furthermore, the K-H surface waves of the water jet are relatively small near the nozzle exit, and larger turbulent flow will appear with increasing flow distance. The growth of the surface waves is mainly the increase of amplitude and wavelength of surface waves, which will be discussed in detail in Sections 4.2 and 4.3.

In our experiment, when the light passes through the water jet, the image intensities at the crests and the troughs of surface waves are different due to reflected light intensity. Variation in image intensities along the flow direction of the water jet can reflect the surface wave characteristics. The wavelength of the water jet surface wave can be calculated by analysis of the intensity signals of these jet images. Firstly, these images must be denoised in order to reduce the noise and improve analysis accuracy of the output signal [25]. The Median filtering is chosen to denoise the jet images in our experiment. Then, Sobel operator is used with a filtering algorithm together to enhance the boundary of the jet image in our experiment. Figure 4 shows the result obtained using the Sobel operator. The overall distribution of horizontal boundary is consistent with the flow direction of the water jet. On the contrary, the vertical boundary is perpendicular to the flow direction of the water jet. Figure 4 shows that the vertical and horizontal boundaries of fire water jet surface waves are enhanced by Sobel horizontal algorithm and vertical algorithm, well. Obviously, the signal strength is enhanced and the resolution is increased by using Sobel operator.

The wave structures on the jet surface are complex and usually involve multiple scales. Much useful information on the image is invisible to our eyes. Analysis of the mutation

on image intensity to detect targets is an effective method [26]. In order to measure the disturbance structures of water jet surface, the image intensity along the water jet flow direction is extracted. As shown in Figure 5(a), a red line of 1 pixel on the symmetrical axis of the image extends in the stream-wise direction. The corresponding image intensity distribution of pixels on this line is shown in Figure 5(b). The fluctuation of the jet surface on the photograph is transformed to image intensity distributions. The curve has obvious periodicity. It also can be seen from the curve that the distance between peaks is increasing, indicating that the wavelength increases gradually along the water jet flow direction. That is to say, jet images are constructed well based upon digital information representing image intensities. Then, power spectral density estimation is used to analyze the periodicity of image intensities variation and calculate the wavelength. As mentioned above, the Burg method is selected to process the jet image intensity, whose results are shown in Figure 5(c).

Based on the above result of data analysis, the wavelength can be calculated as

$$\lambda = \frac{N}{f} \times m \quad (6)$$

where  $\lambda$  is wavelength of surface wave,  $N$  is the count of sample,  $f$  is the count of waves corresponding to position of wave crest, and  $m$  is the resolution of the image. In Figure 5(c), the count of sample is 1000, the wave number corresponding to the maximum spectral peak is 23.4375, and the resolution of the image is  $20 \mu\text{m}/\text{pixel}$ . The wavelength calculated by (6) is 0.853 mm.

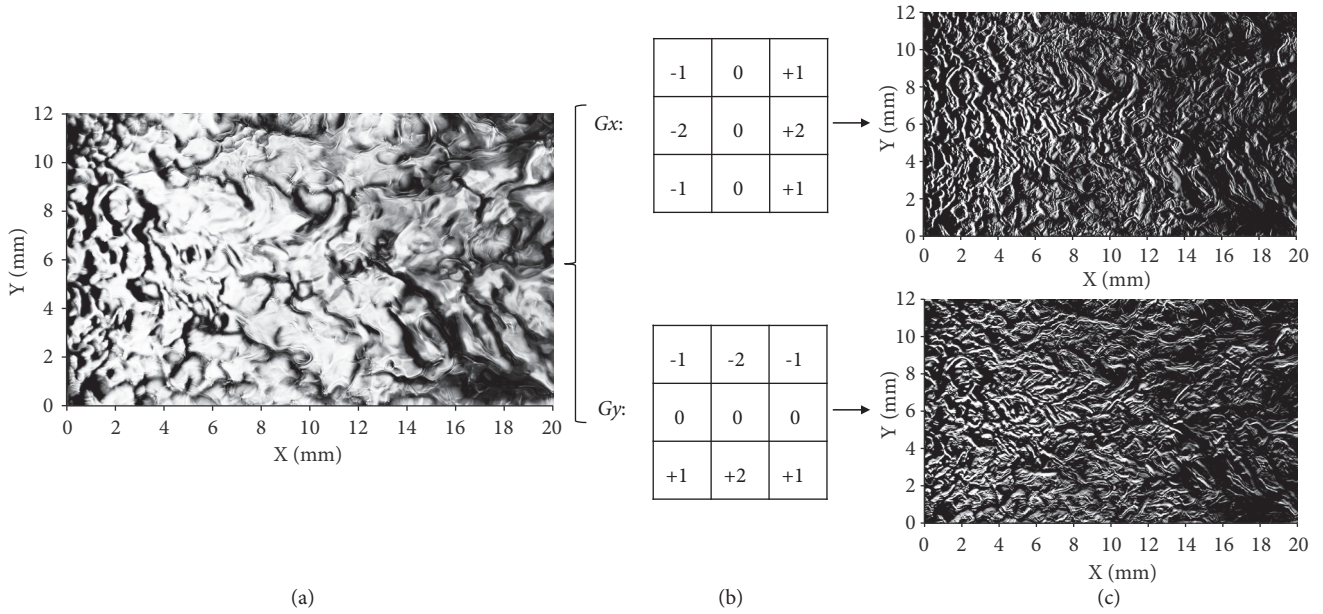


FIGURE 4: Comparisons on Sobel horizontal and vertical gradients. (a) Original image. (b) Horizontal and vertical Sobel masks. (c) Results of horizontal and vertical gradients using Sobel operator.

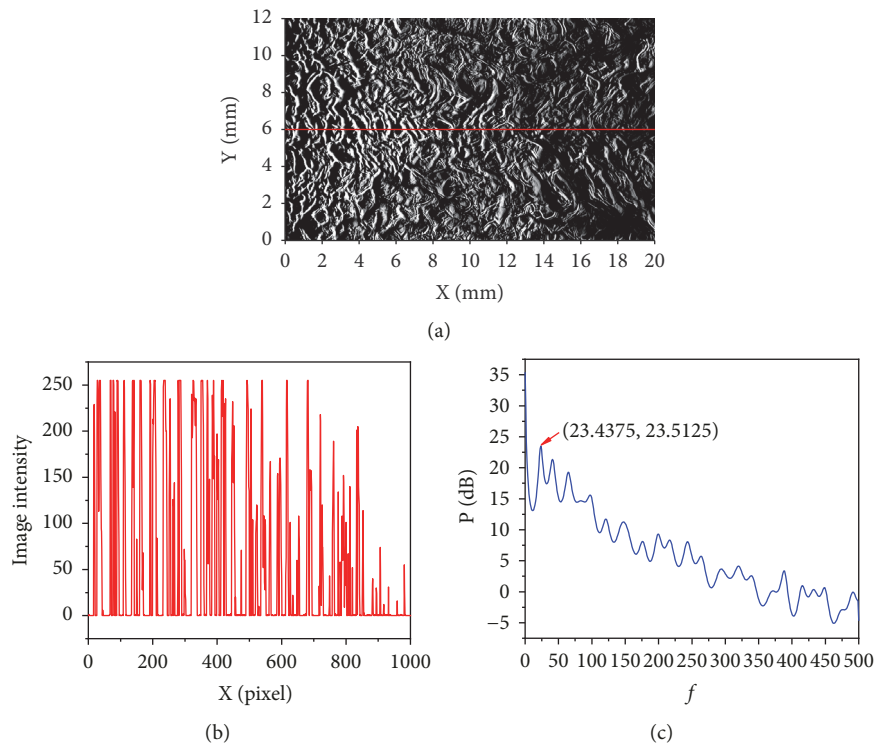


FIGURE 5: (a) A red line of 1 pixel along the jet flow direction on image of vertical boundary. (b) Image intensity distribution of pixels along the red line. (c) Result obtained by the Burg method (the ordinates are the degree of model P, and the abscissa is the count of waves  $f$  corresponding to position of wave crest).

## 4. Discussion

4.1. *Microstructures of Water Jets.* When water is ejected from a nozzle, the surface of water jet is directly in contact with the air, which is no longer restricted by the nozzle

structure. The surface of the water jet fluctuates due to the uneven distribution of velocity caused by the shear stress at the boundary layer between water and air as highlighted schematically in Figure 6. The surface velocity of water jet is approximately 0 at the moment it leaves the nozzle and

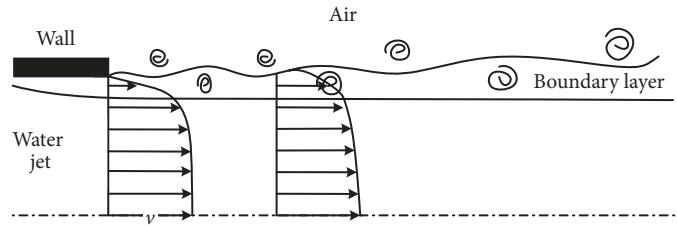


FIGURE 6: Model schematic of surface wave generation and development (not to scale).

increases gradually with increasing velocity, until it is equal to the center velocity of the water jet. With the increasing surface velocity of the water jet, the shear is higher in magnitude, and the vortices will appear in the shear layer [27, 28]. Furthermore, the disturbance caused by the shearing motion appears in the air [11]. Then these vortices and disturbances develop and merge and the K-H surface wave could be found on the water jet.

Figure 7 shows images of the water jets out from fire water monitor captured by the high-speed camera in our experiment. It shows that variations of surface waves along the flow direction under different  $We_g$  are similar. The surface waves of the jet are relatively small near the nozzle exit and fluctuate violently in the downstream of the water jet. As shown in Figure 7, the momentum in the boundary layer is transferred to the interior of the water jet, which promotes gas-liquid two-phase mixing, and promotes the development of surface waves. With the progression of the water jet, the wave structures are stretched in both flow and vertical directions, and larger turbulent eddies are found. With larger flow distance, the complex on the flow structure is increased, the disorder of surface wave is enhanced, and the turbulence intensity is increased. Furthermore, the increasing Weber number has also an important effect on the surface waves. When the Weber number increases from 6.99 to 139.55, the structure of the surface wave changes from cosmic turbulence to stochastic small-scale waves. The turbulence intensity increases on the surface of water jet with increasing  $We_g$ , because the ratio between aerodynamic force and liquid surface tension increases. If the Weber number is lower, the surface tension plays a major role. In contrast, higher Weber number means increasing aerodynamic force, which will accelerate the development of surface wave. And the liquid column becomes more unstable, and the wavelength of surface waves gets shorter. When the  $We_g$  is less than 44.75, some bigger surface waves could be seen by naked eyes. Generally, the wavelength of the surface wave is bigger than that under larger  $We_g$ . While the  $We_g$  is larger than 84.21 and turbulence intensity increases, the surface structures become fully chaotic.

**4.2. Wavelength Characteristic of Surface Waves.** In our experiment,  $Y=6$  mm is the axis of the water jet, so  $Y=4$  mm, 5 mm, 6 mm, 7 mm, and 8 mm of each picture are selected to calculate the average wavelength by (6). Based on the statistical principle, the wavelength of water jet surface waves with increasing  $We_g$  is illustrated in Figure 8. Figure 8

indicates that the average wavelength decreases with the increasing  $We_g$ . The wavelength of water jet ranges from 1.55mm to 0.48mm while the  $We_g$  number increases from 6.99 to 139.55. When  $We_g$  is less than 36, the wavelength of water jet decreases rapidly, and then the rate of decreasing is slowing down. As discussed above, the turbulent intensity in the boundary layer increases with increasing Weber number, which leads to decreasing wavelength of water jet. Furthermore, while the Weber number is lower, aerodynamic force is a low frequency of disturbance. In contrast, higher Weber number means increasing aerodynamic force, and aerodynamic force is a higher frequency of disturbance at this time. This higher frequency of disturbance is intended to diminish the disturbance scale, then leading to the decrease in the wavelength.

Furthermore, the wavelength characteristic vs flow distances of the water jet are presented in Figure 9. The data of image intensity is divided into 4 equal parts and each part has 250 pixels (5 mm) in our experiment. Figure 9 shows that the wavelength of the water jet out from fire water monitor is raising with increasing flow distance when the  $We_g$  is kept constant. The larger the flow distance, the faster the growth rate of the wavelength. Furthermore, the Weber number promotes the development of the surface wave. When the  $We_g$  is smaller, such as 6.99, the increasing rate of wavelength along the jet flow direction is extremely small. Relatively, while the  $We_g$  is larger, such as 112.29, the increasing rate of wavelength along increasing distance is bigger. The reasons are as follows. When the water jet is ejected from a nozzle, the boundary condition of the water jet changes from nonslip boundary condition to free surface. As the surface velocity of the water jet increase from 0, velocity difference between the surface and center of the water jet decreases with increasing flow distance, resulting in the relaxation process of the velocity distribution [20]. At the same time, the turbulent intensity in the boundary layer will change the size of turbulent and the wavelength of the surface wave. The scale of disturbance in the air caused by the shear stress and aerodynamic force expands along the flow direction, which is also the reason of increased wavelength. Furthermore, the ambient air has shear forces opposite to the water jet flow direction, which makes the velocity of surface wave unevenly distributed in the flow direction. So the surface wave with larger velocity upstream merges with lower velocity downstream, resulting in a gradual increase of surface wavelength along the flow direction.

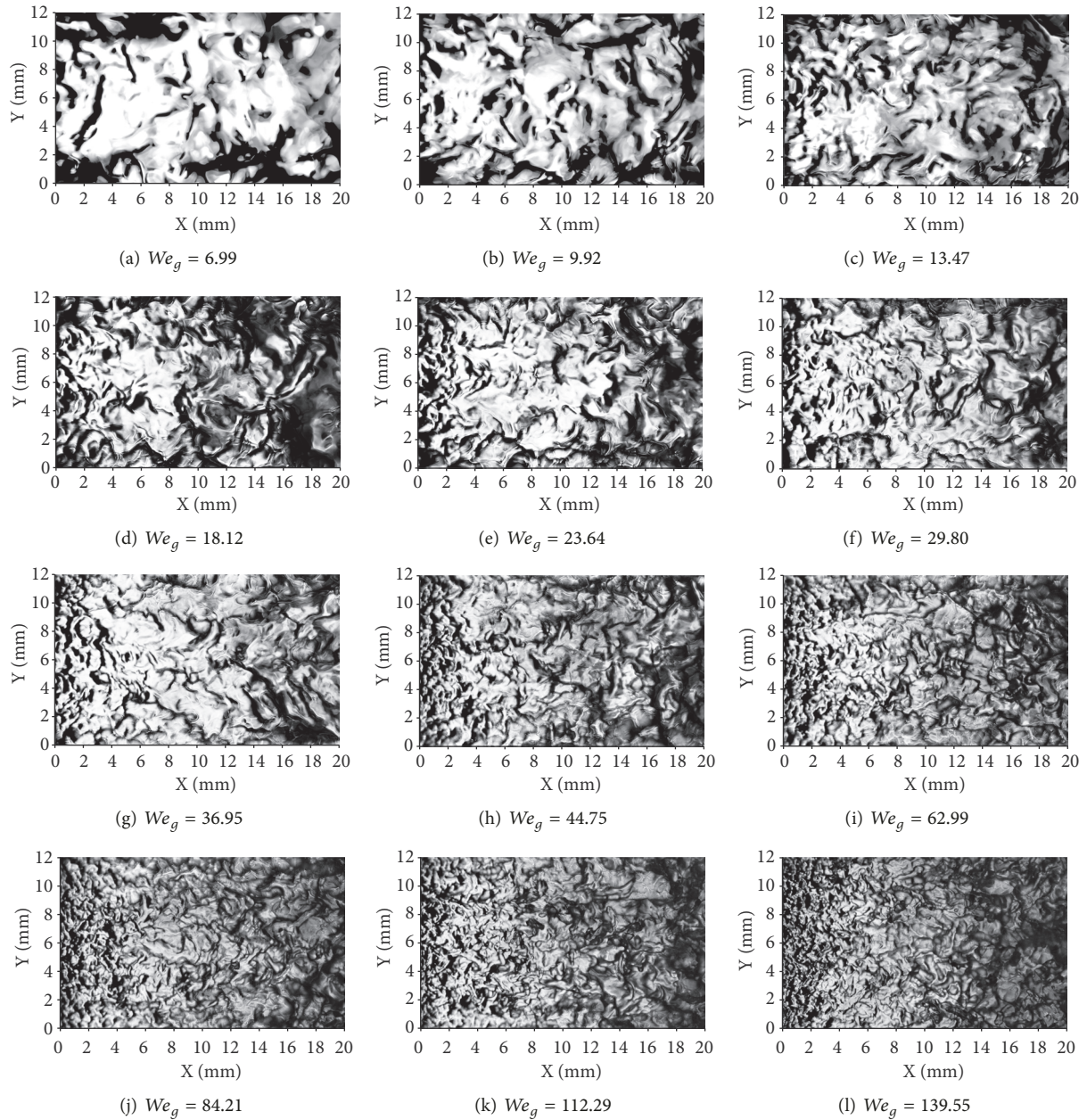


FIGURE 7: Surface waves of fire water jets with different Weber number.

4.3. *Amplitude Behaviors of Surface Waves on Water Jets.* To analyze the spatial and temporal structures of surface waves on water jets in more detail, variations of wave amplitude are presented in Figure 10. The data is acquired by image enhancement and image segmentation of jet images, and then the contour of water jets is extracted and fitted as shown in Figure 3(b). The amplitude of surface wave is calculated as the mean square value of the distance between contour points of the water jet and the fitting line. More detailed discussion about the digital signal processing method could be found in our previous work [29]. Figure 10 indicated that the wave amplitude continues to increase with increasing flow distance, which is due to the continuous extension of water

column in the radial direction. The larger the contact area between the water and air is, the more intense the disturbance is. In addition, the amplitude of surface wave increases with the increase of Weber number. The reasons are attributed to the mentioned strengthened disturbance caused by the shear motion and aerodynamic force.

The spatial distribution of surface waves varies greatly at different times. The contour of the surface wave with the time interval  $266\mu s$  is presented in Figure 11(a), while the Weber number is 36.95. From the graph it can be seen that the contour of surface waves on the water jet does not obviously change within  $266\mu s$ , such that A, B, C, and D correspond to A', B', C', and D', respectively, but the spatial position is

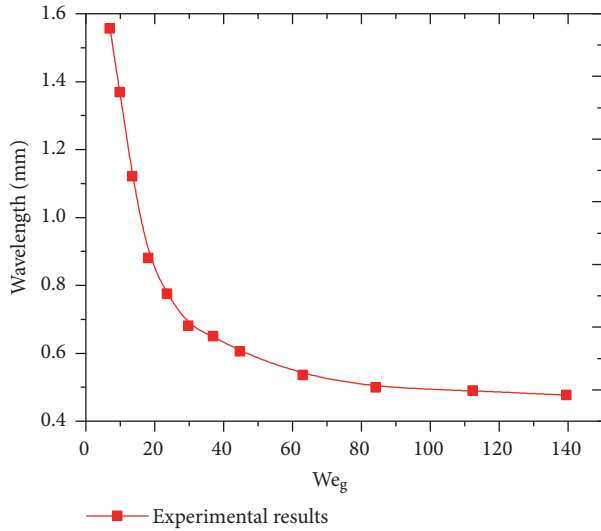


FIGURE 8: The relationship between average wavelength of the water jet and Weber number.

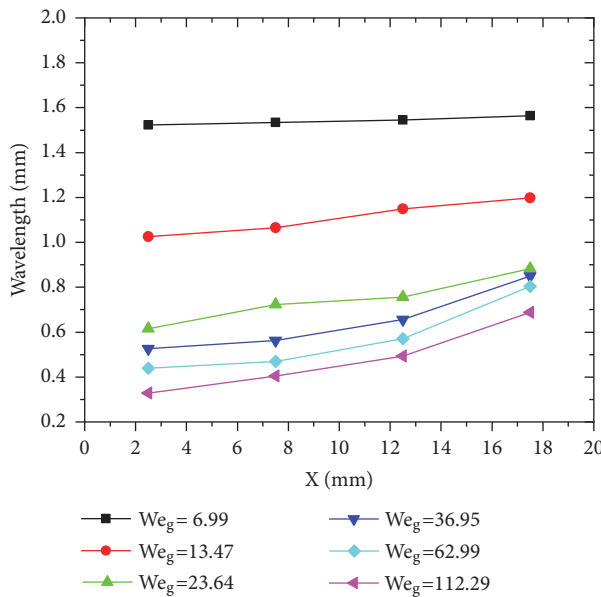


FIGURE 9: Variation of wavelengths with increasing distance and Weber number.

changed and moves downstream at a certain distance. By calculation, we could know that point A on the surface wave moves about 1.30 mm to the right, and the velocity is 4.88 m/s. Point B moves about 1.42mm with a velocity of 5.34 m/s, while C moves about 1.46mm with a velocity of 5.49 m/s, and D moves about 1.60mm with a velocity of 6.02 m/s. The velocity of surface waves on water jets increases with increasing flow distance. Furthermore, the Weber number also has a great relationship with the velocity of surface waves on water jets. Figure 11(b) illustrates the variations of wave velocities at different Weber numbers. It can be concluded that the larger the Weber number is, the faster the velocity of surface waves on water jet is. In other words, the velocity

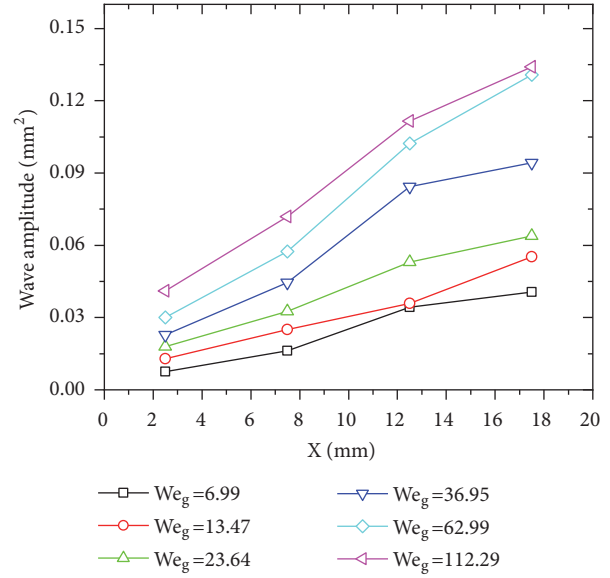


FIGURE 10: Stream-wise variation of wave amplitude.

of surface wave is enhanced by higher Weber number. In addition, the increasing rate of wave velocity increases with the increasing Weber number, which is the same as the increasing law of wavelength.

### 5. Conclusions

Characteristics of the water jet out from fire water monitor are investigated in our paper. A new fire water jet system and a high-speed camera are used to obtain water jet from fire water monitor, and the image intensity along the jet direction is successfully extracted. Image intensity signal of Sobel vertical edge, combined with the Burg method, can be effectively used in the study of the evolution of water jet wavelength in the flow in both time and space. The structure of the surface wave changes from cosmic turbulence to stochastic small-scale waves with increasing Weber number and becomes fully chaotic finally. The wavelength of the water jet increases with the flowing distance. Additionally, the average wavelength is inversely proportional to the Weber number. Surface wavelength of water jet ranges from 1.55mm to 0.48mm, while the  $We_g$  number increases from 6.99 to 139.55. The related physical mechanism has also been discussed. Furthermore, the spatial and temporal structures of surface waves on water jets are also discussed in more detail. The amplitudes of the water jet increase continuously with increasing flow distance. The Weber number also promotes the amplitude and the velocity of surface waves. The larger the Weber number, the faster the velocity and the larger the amplitude of surface waves on water jet.

### Data Availability

The data used to support the findings of this study are available from the corresponding author upon request.

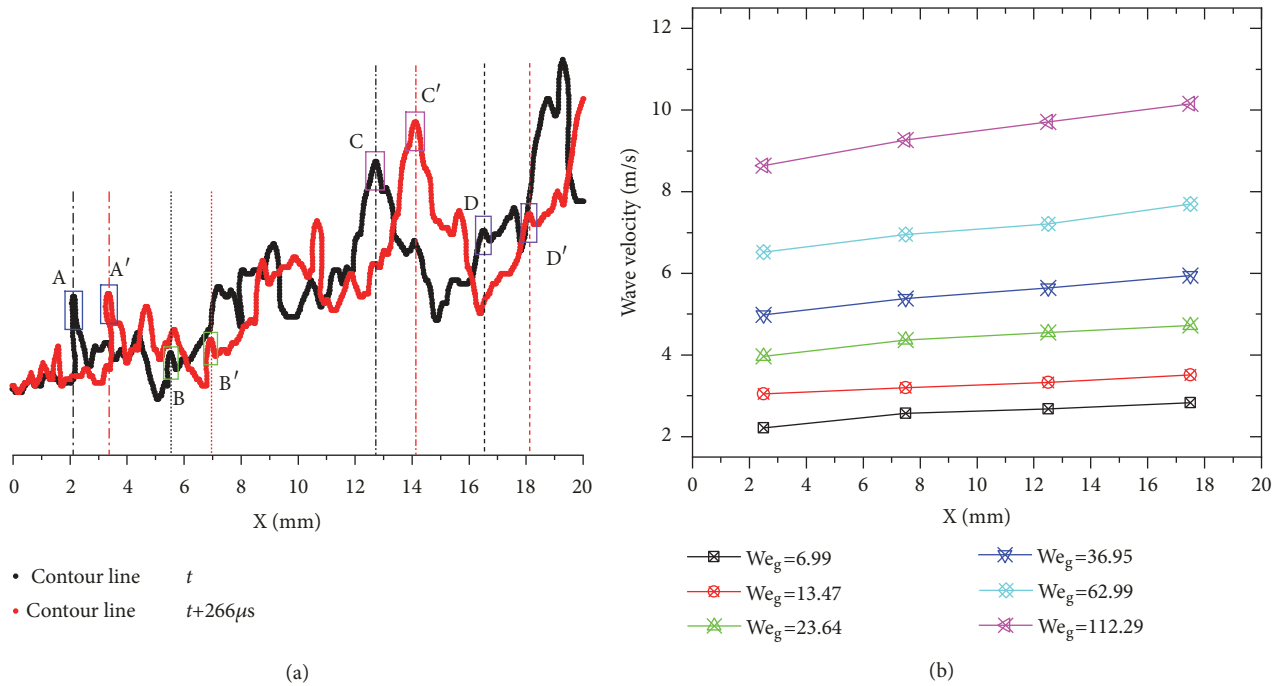


FIGURE 11: (a) Evolution of surface waves on water jets. (b) Stream-wise variation of wave velocity.

**Conflicts of Interest**

The authors declare no conflicts of interest.

**Authors' Contributions**

He Jie and Wang Jingjing contributed equally to this work. Wang Jingjing performed experiments and wrote the draft. He Jie analyzed the data and cowrote the draft. Liu Xiumei designed and supervised the project and revised the manuscript. Li beibei discussed the data. Gu Ming wrote the image processing program. Xie Yongwei, Cai Zonghang, and Ma Jichao helped in carrying out the experiments. Li Wei gave some advices about interpreting the data. All authors discussed the results and implications and commented on the manuscript at all stages.

**Acknowledgments**

This research was funded by the National Key Research and Development Project [grant number 2016YFC0802908]; the National Natural Science Foundation of China [grant number 51875559]; the Natural Science Foundation of Jiangsu Province [grant number BK20171189]; Six Talent Peaks Project in Jiangsu Province [grant number ZBZZ-008] and the Priority Academic Program Development of Jiangsu Higher Education Institutions (PAPD).

**References**

[1] M. C. Leu, P. Meng, E. S. Geskin, and L. Tismeneskiy, "Mathematical modeling and experimental verification of stationary

waterjet cleaning process," *Journal of Manufacturing Science and Engineering*, vol. 120, no. 3, pp. 571–579, 1998.  
 [2] H. V. Tafreshi and B. Pourdeyhimi, "The effects of nozzle geometry on waterjet breakup at high Reynolds numbers," *Experiments in Fluids*, vol. 35, no. 4, pp. 364–371, 2003.  
 [3] T. Miyashita, O. Sugawa, T. Imamura, K. Kamiya, and Y. Kawaguchi, "Modeling and analysis of water discharge trajectory with large capacity monitor," *Fire Safety Journal*, vol. 63, pp. 1–8, 2014.  
 [4] G. L. Hu, A. M. Hu, and J. X. Liang, "Study of the influence rules between structural parameters and jet characteristics of a liquamatic fire water monitor with self-swinging device," *Applied Mechanics and Materials*, vol. 37-38, pp. 1254–1258, 2010.  
 [5] G. Hu, M. Long, J. Liang, and W. Li, "Analysis of jet characteristics and structural optimization of a liquamatic fire water monitor with self-swinging mechanism," *The International Journal of Advanced Manufacturing Technology*, vol. 59, no. 5-8, pp. 805–813, 2012.  
 [6] A. Guha, R. M. Barron, and R. Balachandar, "Numerical simulation of high-speed turbulent water jets in air," *Journal of Hydraulic Research*, vol. 48, no. 1, pp. 119–124, 2010.  
 [7] A. Guha, R. M. Barron, and R. Balachandar, "An experimental and numerical study of water jet cleaning process," *Journal of Materials Processing Technology*, vol. 211, no. 4, pp. 610–618, 2011.  
 [8] S. C. Zhang, X. H. Tao, J. S. Lu, X. J. Wang, and Z. H. Zeng, "Design, optimization and CFD simulation of a nozzle for industrial cleaning processes based on high-pressure water jets," *International Journal of Oil Gas & Coal Technology*, vol. 7, pp. 1–28, 2015.  
 [9] S. C. Zhang, X. H. Tao, J. S. Lu, X. J. Wang, and Z. H. Zeng, "Structure optimization and numerical simulation of nozzle for high pressure water jetting," *Advances in Materials Science and Engineering*, vol. 2015, Article ID 732054, 8 pages, 2015.

- [10] J. Shinjo and A. Umemura, "Simulation of liquid jet primary breakup: dynamics of ligament and droplet formation," *International Journal of Multiphase Flow*, vol. 36, no. 7, pp. 513–532, 2010.
- [11] J. Shinjo and A. Umemura, "Surface instability and primary atomization characteristics of straight liquid jet sprays," *International Journal of Multiphase Flow*, vol. 37, no. 10, pp. 1294–1304, 2011.
- [12] D. Fuster, A. Bagué, T. Boeck et al., "Simulation of primary atomization with an octree adaptive mesh refinement and VOF method," *International Journal of Multiphase Flow*, vol. 35, no. 6, pp. 550–565, 2009.
- [13] H. Ding, Z. Wang, Y. Li, H. Xu, and C. Zuo, "Initial dynamic development of fuel spray analyzed by ultra high speed imaging," *Fuel*, vol. 169, pp. 99–110, 2016.
- [14] S. Yu, B. Yin, W. Deng et al., "Experimental study on the spray characteristics discharging from elliptical diesel nozzle at typical diesel engine conditions," *Fuel*, vol. 221, pp. 28–34, 2018.
- [15] J. G. McNeil and B. Y. Lattimer, "Robotic fire suppression through autonomous feedback control," *Fire Technology*, vol. 53, no. 3, pp. 1171–1199, 2017.
- [16] W. O. H. Mayer and R. Branam, "Atomization characteristics on the surface of a round liquid jet," *Experiments in Fluids*, vol. 36, no. 4, pp. 528–539, 2004.
- [17] Y. Ma, D. Z. Zhu, N. Rajaratnam, and G. A. Camino, "Experimental study of the breakup of a free-falling turbulent water jet in air," *Journal of Hydraulic Engineering*, vol. 142, no. 10, Article ID 06016014, 2016.
- [18] C. L. Ng, R. Sankarakrishnan, and K. A. Sallam, "Bag breakup of nonturbulent liquid jets in crossflow," *International Journal of Multiphase Flow*, vol. 34, pp. 241–259, 2008.
- [19] J. E. Portillo, S. H. Collicott, and G. A. Blaisdell, "Measurements of axial instability waves in the near exit region of a high speed liquid jet," *Physics of Fluids*, vol. 23, no. 12, pp. 47–177, 2011.
- [20] C. Gong, M. G. Yang, C. Kang, and Y. L. Wang, "Experimental study of jet surface structures and the influence of nozzle configuration," *Fluid Dynamics Research*, vol. 48, Article ID 045503, 2016.
- [21] C. Gong, M. Yang, Y. Wang, and C. Kang, "Wavelength measurement of a liquid jet based on spectral analysis of image intensity," *Advances in Mechanical Engineering*, vol. 7, no. 8, pp. 1–10, 2015.
- [22] P. D. Welch, "The use of fast Fourier transform for the estimation of power spectra: a method based on time averaging over short, modified periodograms," *IEEE Transactions on Audio and Electroacoustics*, vol. 15, no. 2, pp. 70–73, 1967.
- [23] C. Gong, M. Yang, C. Kang, and Y. Wang, "The acquisition and measurement of surface waves of high-speed liquid jets," *Journal of Visualization*, vol. 19, no. 2, pp. 211–224, 2016.
- [24] M. A. André and P. M. Bardet, "Interfacial shear stress measurement using high spatial resolution multiphase PIV," *Experiments in Fluids*, vol. 56, pp. 1–18, 2015.
- [25] H. Fan and H. Zhu, "Preservation of image edge feature based on snowfall model smoothing filter," *Eurasip Journal on Image and Video Processing*, vol. 2018, no. 1, 67 pages, 2018.
- [26] Y. Min, B. Xiao, J. Dang, B. Yue, and T. Cheng, "Real time detection system for rail surface defects based on machine vision," *Eurasip Journal on Image Video Processing*, vol. 2018, 3 pages, 2018.
- [27] M. A. André and P. M. Bardet, "Free surface over a horizontal shear layer: vorticity generation and air entrainment mechanisms," *Journal of Fluid Mechanics*, vol. 813, pp. 1007–1044, 2017.
- [28] M. A. André and P. M. Bardet, "Experimental study of shear layer instability below a free surface," *Physics of Fluids*, vol. 27, no. 11, Article ID 112103, 2015.
- [29] X. Liu, J. Wang, B. Li, and W. Li, "Experimental study on jet flow characteristics of fire water monitor," *The Journal of Engineering*, vol. 2019, no. 13, pp. 150–154, 2019.

